Available online at www.sciencedirect.com

Manufacturing Letters

Manufacturing Letters 33 (2022) 692–700

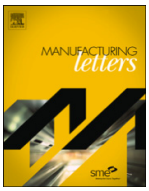

50th SME North American Manufacturing Research Conference (NAMRC 50, 2022)

Tracking and quantifying spatter characteristics in a laser directed energy deposition process using Kalman filter

Ashif Sikandar Iquebal[a,*] Aakash Yadav[b], Bhaskar Botcha[b], Rama Krishna Gorthi[c], Satish Bukkapatnam[b,*]

[a]*School of Computing and Augmented Intelligence, Arizona State University, Tempe, 85281, AZ*
[b]*Department of Industrial and Systems Engineering, Texas A&M University, College Station, 77840, TX*
[c]*Department of Electrical Engineering, IIT Tirupati, Tirupati, 517506, Andhra Pradesh, India*
* Corresponding author. Tel.: +1-979-739-2685, +1-979-458-2348; *E-mail address:* aiquebal@asu.edu, satish@tamu.edu

Abstract

Laser-based directed energy deposition (L-DED) has emerged as one of the most promising additive manufacturing (AM) technologies in the past decade. This is particularly due to its ability to print functionally graded materials and achieve a higher deposition rate compared to its counterparts. For L-DED, the flow dynamics of the powder particles and laser-material interactions are the chief determinants of the build quality. In particular, we are interested in the characterization of spatter, which is the ejection of the molten material from the deposition zone that includes the melt pool and the area where the laser interacts with the incident powder particles. Spatters are detrimental to the overall build quality as they can increase porosity and lead to irregular surface morphology. While recent studies have investigated the spatter formation, very little attention has been given to its quantitative *in situ* characterization. To this end, we develop a high-speed imaging capability integrated with an L-DED process to record the trajectory of the spatter particles as they eject out from the deposition zone. We use a Kalman filter to track the trajectory of the individual spatter particles in real-time. By using the trajectory information and *apriori* knowledge of the material properties, we estimate the percentage of the material lost as spatter. Our results indicate that at a laser power of 300 W and a feed rate of 7.41 mm/sec, only an estimated 11% of the powder material (released from the nozzles) interacts with the laser beam. Out of this, approximately 12% of the material is ejected out as spatter. This shows that a significant portion of the material is wasted during the L-DED process.

Keywords: Directed energy deposition; High speed imaging; Kalman filter; spatter

1. Introduction

The past decade has witnessed rapid growth in metal additive manufacturing (AM) technologies. These include powder bed fusion, binder jetting, laser-based directed energy deposition, and fused deposition modeling. Among these, laser-based directed energy deposition or L-DED has received significant attention largely due to its ability to print functionally graded components with gradation in either X, Y, or Z direction, increased printing speeds as compared to its counterparts, as well as its ability to build on an existing structure, as in repair/remanufacture of damaged components [2]. In addition, high cooling rates (1000-5000° C/s) and large thermal gradients in the L-DED process allow us to control the resulting microstructures and mechanical properties [2].

The L-DED process utilizes a powder feedstock that flows from the spray nozzles and a focused laser beam that intersects with the path of the powder feedstock at the substrate, where deposition occurs. Henceforth, we refer to this intersecting region that is known to form plasma and vapors [3] as a *deposition zone*. The laser, spray nozzles, and a high-pressure gas nozzle are all housed inside a print head (see Fig. 1(a) for reference). As the printing progresses, the print head moves relative to the substrate until the layer is printed. It is important to note that unlike other metal printing methods where laser melts a layer of deposited powder, the L-DED process involves melting the powder particles as they are being sprayed from the

nozzle. Consequently, the dynamics of the powder particles at the point of intersection of the laser and powder particles, including the trajectory, morphology, as well as physical and chemical characteristics, control the final quality and integrity of the parts. The dynamics of how the powder particles are melted and deposited is highly stochastic and depends not only on the laser power but also on the powder size distribution, powder flow rate, material characteristics, and scan speed [4]. A majority of the earlier works have focused on monitoring and modeling the thermal history of the process and not the powder dynamics, which has a significant bearing on the final part quality and properties. While a few thermal and simulation models have been developed to study the dynamics of powder particles [5], they are primarily based on simplified laser absorptivity parameters for the powder feedstock and, therefore, are inefficient at modeling the powder dynamics.

Powder spattering not only leads to material wastage but is also detrimental to the overall part quality. For instance, earlier studies reported that the ejection of molten particles from the deposition zone leads to the formation of keyhole pores [3, 6]. In addition, the spatter particles (often oxidized), regardless of their origin, may deposit elsewhere on the build surface, causing irregular surface morphology and unintended morphological and compositional variability [7]. To develop a comprehensive understanding of the dynamics of the L-DED process, it is crucial to record and quantify the real-time trajectory of the powder particles as they interact with the laser beam. In this work, we are particularly interested in characterizing the dynamics of the spatter particles that are essentially the molten powder particles ejected out from the deposition zone, including the melt pool, during the printing process.

Although not fully understood, different mechanisms for spatter formation has been proposed and speculated for different powder-based additive manufacturing processes. For instance, in L-DED, spatter formation is attributed to the formation of a powder island in the melt pool due to insufficient melting of the powder particles by the applied laser power. Here, the powder particles near the edge of the melt pool form metal droplets, some of which rupture and either incorporate with the melt pool or get ejected as spatter due to the boiling effects or surface tension [8][9]. In the power-bed fusion process, recent works based on high-speed imaging suggest that vapor-driven entrainment and recoil pressure are the two mechanisms through which spatter particles emanate, with the former being the dominant one [6]. The initial theory is the development of a recoil pressure in the melt pool when the temperature exceeds the vaporization temperature of the particles. This creates a recoil pressure, causing rapid motion in the melt pool and eventual ejection of the material. However, more recent works suggest that vapor-driven entrainment where pressure gradient entrains the nearby particles may be the driving force for denuding the powders near a melt track [10]. Nonetheless, as noted earlier, previous works have primarily focused on the qualitative assessment of the spatter particles as observed from high-speed video streams. In contrast, little effort has gone into real-time tracking and statistical analysis of the spatter particles. Therefore, to complement the existing works on understanding the mechanism of material deposition in L-DED and to bridge the gaps in the literature, we present quantitative characterization of spatter.

To this end, we employ a high-speed camera (operating at 1000 frames per second) to record the dynamics of the laser-powder interaction during L-DED printing with SAE 316L stainless steel powders. We first present a video processing approach based on Kalman filter to track and count the number of spatter particles that are ejected out of the melt pool. Our methodology includes a sequence of filtering, binarization, and spatter detection followed by a Kalman filter to predict the trajectory of every spatter particle in real-time. By doing so, we estimate the rate of spatter generation observed over a period of 30 seconds. Our investigations suggest that at a laser power of 300 W and a feed rate of 7.41 mm/sec, approximately 11% of the incoming material from the nozzle interacts with the laser beam. The remaining material is scattered without interacting with the laser. Out of the 11% of the powder that interacts with the laser, approximately 12% is ejected via spattering. While these results show that a significant portion of the material is wasted during the deposition process, it also opens an opportunity to improve the mechanical and structural properties of the printed components by controlling the process parameters that can potentially reduce the powder spatter.

The rest of the manuscript is organized as follows: Section 2 presents a review of the literature focused on monitoring of general AM processes followed by the recent efforts, particularly in the L-DED process. In Section 3, we present the experimental details. Section 4 discusses the video processing and the Kalman filter used in this work. Results and analysis of the spatter particles obtained from this study are presented in Section 5, followed by discussions and conclusions in Section 6. We also provide limitations of the present work and ideas for future studies.

2. Literature review

In situ monitoring of AM processes has been widely studied using non-contact thermal measurements via pyrometers such as photodiodes and infrared imaging, contact thermal measurements via thermocouples, as well as digital and high-speed cameras. In this section, we first provide a general overview of sensing and monitoring approaches in various additive manufacturing processes and then provide an in-depth review of process monitoring in L-DED.

Research on *in situ* monitoring began in the early 1990's beginning with Melvin III *et al.* [11] developing a video microscopy system to observe the sintering and flow behavior of polymer and metal materials in real-time. Subsequently, the monitoring data was employed for real-time defect mitigation and AM control. For instance, Kruth *et al.* [12] presented the online monitoring of electromagnetic radiation emitted by the process using a wide array of sensing technologies such as CCD cameras and single-point photodiodes. Using the real-time data, the authors were able to detect the deterioration in the surface roughness in the selective laser melting (SLM) process. Schwerdtfeger *et al.* [13] employed a similar approach based on infrared images to track the flaws in the deposition quality in an electron beam melting (EBM) system. These

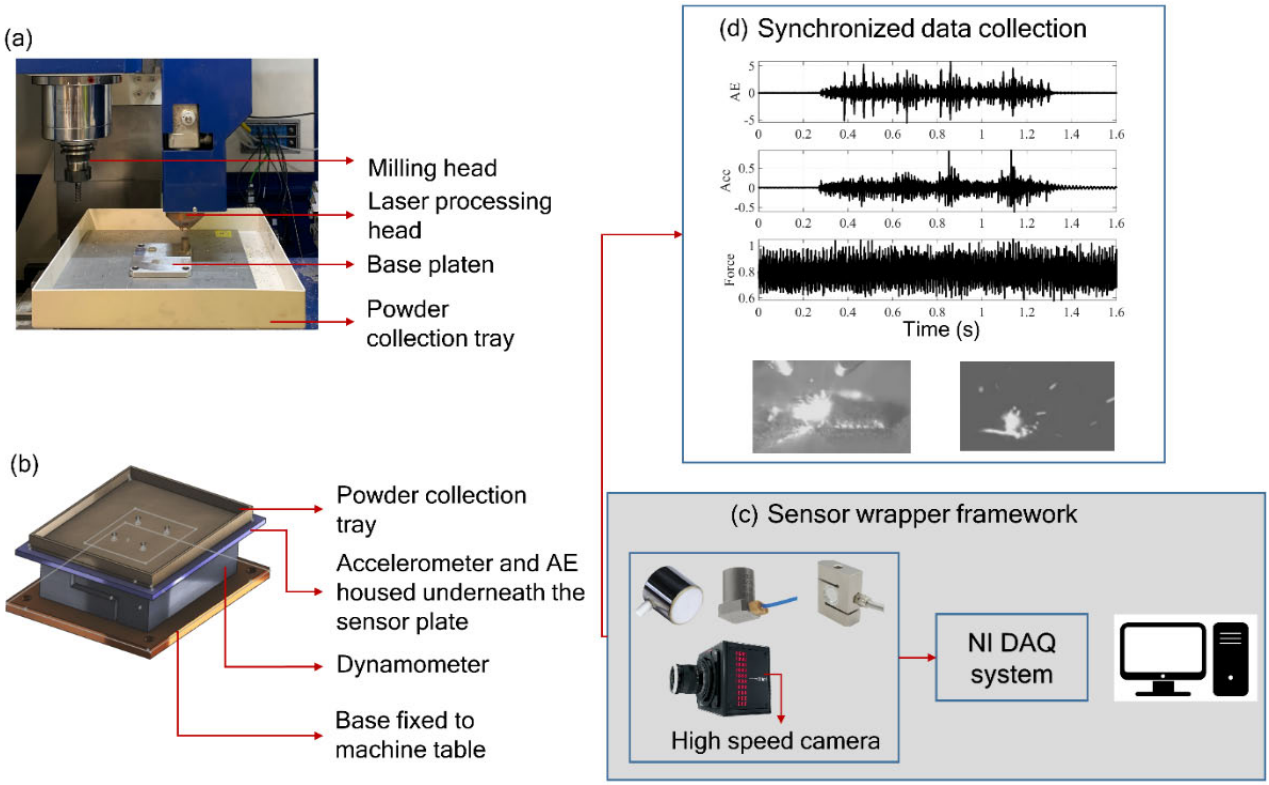

Fig. 1. (a) shows the print head and the milling head within the OPTOMEC hybrid machine integrated with the acoustic emission sensor, accelerometer, and force sensors, all housed under the enclosure shown in (b). Using an NI-DAQ system, the data collected from all the sensors and the high-speed camera are synchronized for to enable synchronous tracking of the L-DED process [1].

indirect measurements of the build quality showed promising results and were subsequently studied by authors in [14, 15] to track the melt pool temperature.

While the initial works relied on a stationary sensor configuration to track the deposition process, later works, e.g., Lott *et al.* [16], employed a CMOS camera, mounted coaxially with the laser beam, to track the melt pool as the melt pool was created. To enable high-accuracy measurements, researchers have also employed multi-sensor setups. Chivel and Smurov [17] employed a CCD camera and a two-channel pyrometer to develop a temperature monitoring system. The setup gathered optical measurements of the temperature distribution using the CCD camera in the sintering zone as well as the maximum surface temperature in the irradiation spot using the two-channel pyrometer. Similarly, Clijsters *et al.* [18] developed an optical sensor setup consisting of two optical sensors, a photodiode, and a near-infrared thermal CMOS camera, connected to a field-programmable gate array that collects the melt pool images and transmits the images for processing, in tandem (with sampling frequency above 10 kHz). Using a data analysis system, the time domain measurements were converted to spatial measurement to enable monitoring. The monitoring setup was subsequently employed to detect the formation of defects and porosity in real-time. However, due to limited resolution, the setup was only able to identify large pores (with diameter of the order of 1 mm). Hua *et al.* [19] employed a two-color infrared thermometer to track the effect of powder feed rate and laser power on the melt pool uniformity. Montazeri *et al.* [20] employed a multispectral photodetector to capture the optical emission signatures during the build in a laser powder bed fusion additive manufacturing. The authors extracted the spectral features gathered from the resulting graphs and subsequently a machine learning algorithm to classify the layers into porosity and non-porosity.

Monitoring and control of the laser power based on the temperature measurements have also been employed in the L-DED process. Similar to the EBM and the SLM process monitoring, early research into monitoring the flow characteristics and powder involved the use of photodiodes and low-power lasers. For example, Bi *et al.* [21] employed an IR-temperature sensor to monitor and control the laser power by changing the laser focus to allow homogeneous deposition of the powder material. Tang *et al.* [22] developed a custom powder dispensing head to estimate the powder mass flow rate coupled with a powder flow rate control system and an infrared emitter. By mapping the output of the infrared emitter to the powder flow rate, authors were able to estimate and control the powder flow rate. Hofmeister *et al.* [23] used a CCD camera placed coaxially to the laser beam to obtain the images of the melt-pool. These images were subsequently utilized to study the cooling rates during the deposition process. However, most of these works focused on the monitoring of the melt-pool dynamics, build quality, or the powder flow rates. Chen et al. employed an *in-situ* and *operando* synchrotron X-ray radiography to record the laser-matter interaction and its influence on the melt-pool geometry and dynamics [24]. Nassar et al. integrated a spectroscopy-based imaging technique into L-DED to monitor the geometry of the plume during the deposition of Inconel 718[25] . The authors showed that the

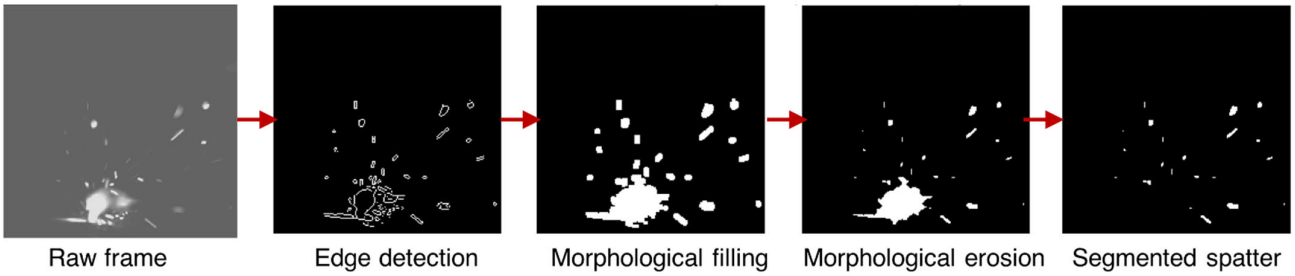

Fig. 2. A sequence of images showing the processing of the raw video frames for detecting the spatter particles. The process involves edge detection followed by morphological filling and erosion. The final step involves removing the region representing the melt pool to obtain the individual spatters.

plume geometry could potentially be used as a surrogate to monitor and control the deposition process.

Given the dynamics of the L-DED process, monitoring the powder flow dynamics, including its trajectory and morphology, is a *sine qua non* to ensuring the quality of deposited layers and eventually the final component. In this direction, Ermurat *et al.* [26] employed a high-speed camera, recording at 20,000 frames per second to monitor the powder flow rate in an L-DED process. Using image analysis methods, the authors were able to deduce the speed of the powder particles emanating from the nozzles. Using this approach, the authors also showed that the standoff distance (distance between the substrate and nozzle) and the gas flow rate had a positive correlation with the particle speeds. Balu *et al.* [27] employed luminance intensity as gathered from high-speed CCD cameras to estimate the powder particle concentration. Using this approach, the authors studied the effect of gas flow rate on the powder concentration for different powder types and compositions.

More recently, Haley *et al.* [28] employed a high-speed camera (with a sampling frequency of up to 200,000 frames per second). Video monitoring allowed the researchers to conclude that the powder particles often float on the surface of the melt pool for several hundreds of microseconds before subsuming into the melt pool. They also studied the trajectory of the incoming particles and observed the rebounding of incoming particles, and thereby deduced that the floating particles create a melt pool shielding, causing a decrease in the powder capture efficiency and increase in the powder rejection. Similar observations were made by Wolff *et al.* [3], where the authors designed a piezo-driven powder delivery system to monitor the dynamics of the powder particles. While the piezo-driven powder delivery system was limited to one-tenth of the mass flow rate in a commercial L-DED process, the authors employed higher scan speeds to trade-off the effect of limited powder flow rate, therefore, mimicking the actual L-DED process. Using a high-speed camera system (frame rate of 20 kHz), the authors studied the trajectory and dynamics of the powder flow with/without interaction with the laser path in the L-DED process and its influence on the porosity formation. Along the same lines, Naesstroem et al. [8] employed a high-speed camera with 10,000 frames per second to monitor the melt-pool in the L-DED process. The authors reported the formation of an island of unmelted powders in the melt pool and the formation of spatter. The formation of the powder island was attributed to the insufficient laser power density. This powder island is also deemed responsible for the formation of spatter in the L-DED process. Authors speculated that the powder grains fed into this island ricochet out of the melt pool, further reducing the capture efficiency of L-DED. Jeon et al. [29] used a coaxial infrared camera in real-time within an L-DED system along with a neural network model to determine the depth of the melt-pool. In addition to the existing works, the current authors also presented a sensing system built as part of a smart manufacturing multiplex [30]. The authors integrated various sensing capabilities such as high-speed imaging, acoustic emission, vibration, and forces to track the powder deposition as we as machining operations within a hybrid additive-subtractive manufacturing system.

In addition to the real-time monitoring approaches, several simulation models have also been developed [31]. Katinas et al. [32] developed a numerical model for the particle trajectory and velocity in L-DED (Optomec LENS 750), which was subsequently used to determine the capture efficiency. Authors showed that for laser power of 350 W, a scan speed of 14.82 mm/sec, and a powder feed rate of 142 mg/sec, the powder capture efficiency (i.e., the ratio of mass added to the build to the mass of the material fed to the nozzles) was only 7.7%. The model was subsequently employed to determine the capture efficiency of direct laser deposition for a single track deposition of Ti-6Al-4V in [33]. In another work, Liu et al. [34] found the powder deposition efficiency to be 10.88% in L-DED using an analytical model based on the net powder flow at any given point and the powder flow rate of individual nozzles. The deposition efficiency was then calculated as the ratio of the mass of the build part to the net powder supplied. However, a critical limitation of numerical models is that they are based on several assumptions on the distribution, size, and shape of the powder particles. Given the limitations of simulation models combined with the computational complexity and inefficiency at capturing the stochasticity of the powder dynamics, we do not delve into summarizing the literature but refer the readers to [35]. Nonetheless, research in the area of monitoring powder dynamics is still in its infancy. To advance the knowledge in understanding the powder dynamics and its impact on the deposition quality, we employ a high-speed, high-resolution camera set up to track the powder particles after ejected from the spray nozzles. We subsequently present an image stream/video processing approach to extract information on the powder dynamics, including the trajectory and the particle count that rebounds from the melt-pool.

3. Experimental Setup

In this work, we utilize a hybrid manufacturing platform that employs L-DED for the additive part with an IPG YLR-1000 fiber laser with a spot size of 600 μm and a wavelength of 1070 nm to melt, fuse, and deposit the metal powder (LENS 500 MTS HM system) [36]. The deposition process was conducted in an open environment condition. The process parameters of the L-DED process were set to laser power = 300 W, hatch spacing of 0.59 mm, and scan speed 7.41 mm/sec. During each cycle a 10 mm × 10 mm × 10 mm cube was printed with 316L SS powder of size 40-150 μm with layer thickness fixed to 300 μm. The hybrid manufacturing platform [37] is instrumented with various high-resolution sensing technologies, including acoustic emission (Physical Acoustics WSA wideband sensor), accelerometer (K-Shear 8728A500), and a tri-axis dynamometer (CNIC Electric Co. MFS15050 with IP67 rated protection) integrated with a National Instruments data acquisition (DAQ) system. A monochrome camera from Photron (Photron Mini AX100) with a Micro-Nikkor VR lens is used to capture high-speed footage of the printing as well as the machining process, as desired. A separate high-intensity light source, Zaila (Make: Nila), with 3200 lumens light output, was used for better illumination. The camera, along with the light source, was placed immediately outside the build chamber to reduce the impact of the laser power. Two different types of imaging are performed, one without using any filters while the other uses the IR filter. We employed an Edmund Optics IR pass filter with a cut-on wavelength of 720 nm and a cut-off wavelength of 2750 nm. In the remaining analysis, we primarily focus on the video captured using the IR filter.

4. Video processing and particle detection

As mentioned in the preceding, we are interested in the spatter particles in an L-DED process. Excessive spatter formation leads to material wastage and results in the deterioration of the build quality. Hence it becomes imperative to reduce the resulting spatter. Monitoring the spatter particles is crucial to understanding the effect of the process parameters on the spatter formation as well as its impact on the build quality.

In order to set and control the process parameters correctly in real-time, we considered the count of the ejected spatter as the output parameter. The counting of the spatter takes place in two stages; first, the spattered particles are detected in each frame, followed by the actual counting of the spatter using appropriate algorithms. The following two subsections talk about this in detail.

4.1 Object detection

We employ methods from image processing to identify the spatters from each of the frames. The approach essentially involves edge detection followed by morphological image processing methods to ensure that the detected objects are noise-free. The first step is detecting the edges of the spatter. In this work, we subscribe to a standard Sobel operator. Once the edges are detected, we employ morphological operations. These operations are used to remove noise, imperfections, and distortions to extract essential artifacts. We first apply morphological filling of the detected contours (that represent particles) using morphological reconstruction via erosion (see [38] for details). Subsequently, we remove any noisy pixels using the erosion operation. The operation involves removing the small, connected components using a structuring element. The components that are smaller than the structuring element are removed during the erosion. The steps are shown in Fig. 2. Similarly, the spatter in each of the frames is detected. In the next step, we employ the Kalman filter to predict the trajectory of the spatters identified thus far.

4.2 Trajectory prediction using Kalman filter

Kalman filter has found widespread application in the computer graphics domain, such as tracking the trajectory of particles/objects using image streams and videos [39]. In simple terms, Kalman filter is a set of mathematical equations that allows predictor-corrector type estimation of the unknown state variables. The approach is based on minimizing the error covariance and is, therefore, optimal. Tracking the spatter has two main challenges. First, the particle locations as recorded by the camera are noisy, especially when the spatter particles get outside the camera's focal plane. As a result, the true center of the spatter particle may not be the same as the center of the spatter as captured by the camera. Second, the spatter particles are not continuously monitored, particularly when another spatter particle comes in front of another particle. As a result, we don't have access to continuous measurements of the particle location. Kalman filter is well suited in such as scenario as it allows us to model the particle position as a function of the previous locations while simultaneously incorporating the uncertainty in the measurements [40].

In this section, we develop the Kalman to estimate and predict the spatter particle trajectory. In this regard, let us denote the state of each of the spatter particles, i.e., the coordinates in two-dimension, by $\boldsymbol{x}_k$ as observed in the k^{th} frame of the image stream. The trajectory of individual spatter particles, or the state of the process is, therefore, a random process that needs to be estimated and can be written in the following form:

$$\boldsymbol{x}_{k+1} = \boldsymbol{\phi}_k \boldsymbol{x}_k + \boldsymbol{w}_k \tag{1}$$

where $\boldsymbol{\phi}_k$ is some transition matrix and $\boldsymbol{w}_k$ is the Gaussian noise with some known covariance function. Observations $\boldsymbol{z}_k$ are made at discrete time points k and is denoted as:

$$\boldsymbol{z}_k = \boldsymbol{H}_k \boldsymbol{x}_k + \boldsymbol{v}_k \tag{2}$$

where $\boldsymbol{H}_k$ captures the relationship between the input state vector $\boldsymbol{x}_k$ and the output measurement $\boldsymbol{z}_k$. The last term represents the white measurement noise. We assume the following structure for $\boldsymbol{v}_k$ and $\boldsymbol{w}_k$:

$$E[\boldsymbol{w}_k \boldsymbol{w}_i'] = \begin{cases} \boldsymbol{Q}_k, i = k \\ \boldsymbol{0}, i \neq k \end{cases} \tag{3}$$

$$E[\boldsymbol{v}_k \boldsymbol{v}_i'] = \begin{cases} \boldsymbol{R}_k, i = k \\ \boldsymbol{0}, i \neq k \end{cases} \tag{4}$$

$$E[\boldsymbol{w}_k \boldsymbol{v}_i'] = \boldsymbol{0}, \forall i, k \tag{5}$$

At any time t_k, let us consider that the estimate of the process state is denoted as $\hat{\boldsymbol{x}}_k^-$ such that the error in the estimate is defined as:

$$\boldsymbol{e}_k^- = \boldsymbol{x}_k - \hat{\boldsymbol{x}}_k^- \quad (6)$$

with the covariance matrix denoted by:

$$\boldsymbol{P}_k^- = E[\boldsymbol{e}_k^- \boldsymbol{e}_k'] \quad (7)$$

The estimate $\hat{\boldsymbol{x}}_k^-$ is made based on the *apriori* knowledge available thus far. However, once the measurement $\boldsymbol{z}_k$ is observed, we seek to update the current best estimate of the process state. This is achieved using the following update equation:

$$\hat{\boldsymbol{x}}_k = \hat{\boldsymbol{x}}_k^- + \boldsymbol{K}_k(\boldsymbol{z}_k - \boldsymbol{H}_k\hat{\boldsymbol{x}}_k^-) \quad (8)$$

where $\hat{\boldsymbol{x}}_k$ is the corrected or the posterior estimate of the process state and $\boldsymbol{K}_k$ is referred to as the Kalman gain which needs to be estimated. To estimate the Kalman gain, we use the method of least squares, i.e., we aim to minimize the error covariance matrix $\boldsymbol{P}_k$ calculated using the corrected estimate of the process state given as:

$$\begin{aligned}\boldsymbol{P}_k &= E[\boldsymbol{e}_k \boldsymbol{e}_k'] \quad (9)\\ &= E[(\boldsymbol{x}_k - \hat{\boldsymbol{x}}_k)(\boldsymbol{x}_k - \hat{\boldsymbol{x}}_k)']\end{aligned}$$

Using the expression of $\boldsymbol{z}_k$, we rewrite the $\boldsymbol{P}_k$ as follows: Upon simplification, the error covariance matrix can be written as:

$$\boldsymbol{P}_k = (\boldsymbol{I} - \boldsymbol{K}_k\boldsymbol{H}_k)\boldsymbol{P}_k^-(\boldsymbol{I} - \boldsymbol{K}_k\boldsymbol{H}_k)' + \boldsymbol{K}_k\boldsymbol{R}_k\boldsymbol{K}_k' \quad (10)$$

We now have an optimization problem where the objective is to determine the value of $\boldsymbol{K}_k$ that minimizes the expression on the right-hand side of Eq. (10). Since the noise process (as noted in Eq (1) is uncorrelated, minimizing Eq (10) amounts to minimizing the individual terms along the diagonal of $\boldsymbol{P}_k$. Using the method of derivatives, we get the optimal value of $\boldsymbol{K}_k$ as:

$$\boldsymbol{K}_k = \boldsymbol{P}_k^-\boldsymbol{H}_k'(\boldsymbol{H}_k\boldsymbol{P}_k^-\boldsymbol{H}_k' + \boldsymbol{R}_k)^{-1} \quad (11)$$

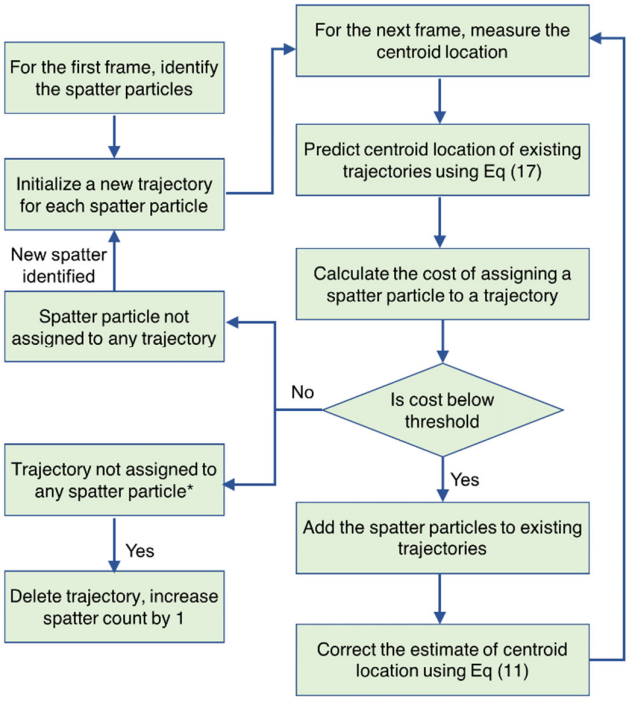

Fig. 3. flow chart of the spatter particle detection algorithm. (*the threshold for marking trajectories as lost is one frame, but can be modified as needed)

We now use the estimate of Kalman gain to update the error covariance matrix. Referring to Eqs. (10) and (11), we now have the updated estimate of $\boldsymbol{P}_k$ as:

$$\boldsymbol{P}_k = (\boldsymbol{I} - \boldsymbol{K}_k\boldsymbol{H}_k)\boldsymbol{P}_k^- \quad (12)$$

The corrected estimate of the process state $\hat{\boldsymbol{x}}_k$ and the error covariance matrix $\boldsymbol{P}_k$ maybe employed to get their best estimate (or one-step prediction) for the next step $k+1$ as:

$$\hat{\boldsymbol{x}}_{k+1}^- = \boldsymbol{\phi}_k\hat{\boldsymbol{x}}_k \quad (13)$$

$$\boldsymbol{P}_{k+1}^- = \boldsymbol{\phi}_k\boldsymbol{P}_k\boldsymbol{\phi}_k' + \boldsymbol{Q}_k \quad (14)$$

The iterative approach for estimating and correcting the process state, therefore, forms the Kalman filter.

4.3 Tracking multiple particles using Kalman filter

The algorithm for tracking multiple particles from the IR video involves an iterative process of initializing and predicting trajectory for individual particles using Kalman filter, updating the trajectories based on the most recent information, and finally deleting the lost trajectories. We describe the algorithm step-by-step in the following.

***a) Initialization*:** For the first ten frames, we identify the spatter particles using the object detection method described in Section 4.1. At this point, the centroid location of each of the spatter particles is stored. Corresponding to each of the spatter particles detected, we initialize a trajectory.

b) Trajectory assignment: For the subsequent frames, the spatter particles are assigned to either already initialized trajectories or new trajectories are initialized. For every spatter particle detected in frame $k+1$, the corresponding centroid location is measured. Simultaneously, we use the Kalman filter to obtain an estimate of the process state $\hat{\boldsymbol{x}}_{k+1}^-$ as given in Eq. (13). We compare the measured centroid location with the estimated centroid locations using the Kalman filter. Each spatter particle i observed in frame $k+1$ is now assigned to the trajectory that minimizes a cost function based on the predicted and measured centroid location given as:

$$\mathcal{L}(\hat{\boldsymbol{x}}_{k+1}, \boldsymbol{x}_{k+1}) = ||\,\hat{\boldsymbol{x}}_{k+1} - \boldsymbol{x}_{k+1}||_2 \quad (15)$$

If the cost of assigning a spatter particle is higher than a pre-specified threshold, then the spatter particle is not assigned. Rather, a new trajectory is initialized. Notice that the threshold for assigning the particles to a particular trajectory is crucial as small values of this threshold will result in too many new trajectories. In contrast, too high of a value may result in the assignment of spatter particles otherwise belonging different trajectories to the same trajectory. In this work, we experimentally found that the value of 20 pixels (the method

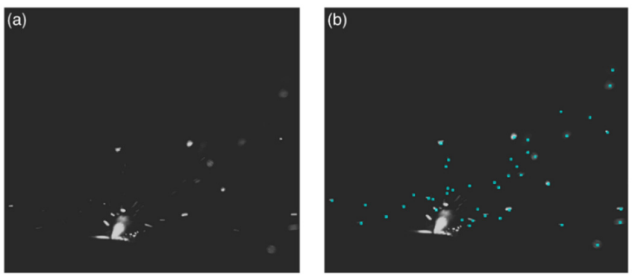

Fig. 4. snapshot(a) of the deposition process and (b) the corresponding detected spatter marked in blue colour.

appears to work well with 15-25 pixels) for the threshold distance resulted in consistent detection of the trajectories.

c) Correction: Once the detected particles are assigned and new measurements are made, the Kalman filter is invoked to correct the estimate of the process state using Eq (8).

d) Counting: If no particles are assigned to a trajectory for more than ten frames, we mark the trajectory as lost trajectories. This is when the particles go out of the frame or disappear as a result of evaporation. Every time a trajectory is lost, we update the spatter particle count by one.

A summary of the whole procedure is also presented in Fig. 3. Before implementing the method, we characterized the spatters emanating from the melt pool into two categories based on their intensity profiles. First, spatters with a bright intensity profile and travels at a rapid pace with a projectile-type trajectory. The second type is the ones that are dull and often appear floating in a disoriented trajectory. The second type of spatters represents the characteristics of plumes that are generated from the melt pool. This observation is similar to the observations made by authors in [41]. For the spatter count, we ignore the second type of particles. We now present the results obtained after implementing the Kalman Filter.

5. Results

5.1. Results from the video analysis

The algorithm was implemented in MATLAB R2017b. Figs. 4(a) and 4(b) show a snapshot of the detection. While it is difficult to estimate the accuracy of detection, we notice that almost all the spatter particles are accurately detected by the algorithm while excluding the central spark zone where the melt pool resides. Note that there are some spatters close to the melt pool that are not detected in this frame. This is because the Kalman filter uses the first ten frames to learn the most likely trajectory of the spatter particle, i.e., for training purposes. These spatter particles are detected in the subsequent frames. Also, note that the spatter particles emerging from the other side of the melt pool may be occluded in the first few frames but would emerge eventually. However, the effect of occlusion is minimum and is not considered in the current study.

The algorithm was used to track the spatter particles for 10,000 frames, i.e., approximately 333 seconds. The total number of spatter particles counted during this time frame was 5412. This translates to approximately 16 spatter particles on an average per second. Note that we also tried two other particle tracking methods: i) based on counting the number of particles leaving a circular boundary around the melt-pool and ii) tracking the particles based on their velocity vector (See Appendix A for discussion on these methods). However, simple tracking methods led to either missing spatter particles or conflict of two or more particle trajectories. As a result, the spatter count was relatively lower when using either of these methods. For the former, we get approximately nine spatter particles per second using the method based on the circular boundary and 11 spatter particles per second using the method based on the velocity vector.

We now convert this count to the mass of the spatter particles. We first summarize the material characteristics needed for the spatter mass calculation. The material used in this study is stainless steel 316L powders with mass density in the molten state to be 8000 kg/m^3 . However, the mass density of the printed parts was estimated to be ~7400 kg/m^3. This is apparently due to porosity arising from the L-DED process (see Fig. 5 for reference). Also, from previous studies such as [42], we note that the spatter size is typically three times to that of the powder particle size. Using the size of powder particles which is in the range of 45-150 μm, we estimate that the spatter size lies in the range of 135 – 450 μm. For this size estimation, we only considered the spatters that have bright intensity profiles. In the absence of any specific measurements, we use the range rule to estimate the mean of the spatter size. The rule says that the mean is one-half of the sum of the maximum and the minimum value. Therefore, the mean diameter of the spatter particle size is 292.5 μm. Using the mass density and the volume of the spatter, we calculate the mass flow rate of the spatter particles as:

$$\mu = \frac{5412}{333} \times 7400 \times \frac{4}{3}\pi \times \left(\frac{292.5 \times 10^{-6}}{2}\right)^3 \times 10^6 \text{ mg/sec}$$
$$= 1.58 \text{ mg/sec}$$

Next, we estimate the mass flow rate for the current L-DED process by collecting the powder particles in a container for one minute. The collected powder particles are then weighed, and the powder mass flow rate was determined to be 124.08 mg/sec. We now estimate the amount of the material that enters the melt pool and then estimate the proportion of the material that is ejected out as spatter.

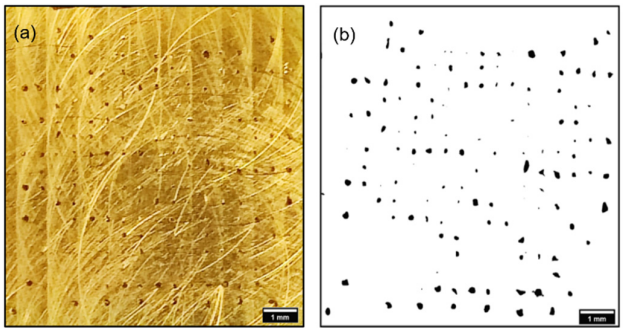

Fig. 5. (a) Optical micrograph showing the porosity on the cross-section of a printed part. The image shows machining marks as we did not polish the cross-section to avoid closure of pores due to localized material redistribution (b) binarized image showing the pores. Based on the binarized image, using image processing, we found the surface porosity to be approximately 7%.

5.2. Material wastage in L-DED

While the previous subsection suggests that approximately 1.58% of the material is ejected via spattering, we need to consider the amount of material that is scattered even before the particles enter the deposition zone. The printed part is of 10 mm × 10 mm × 10 mm and weighs approximately 7400 kg/m^3 × 10^{-6} m^3 ≈ 7.4 g. To estimate the effective material flow rate utilized for printing the part, we first use the scan speed to estimate the print time. In this case, we set the scan speed to 7.41 mm/sec. Each layer involves 17 passes and there are a total of 27 layers. Note that the dwell time was zero and

so the laser was turned off only for the time when it went to zero location after finishing each layer. However, this time was negligibly smaller compared to the layer print time and so ignored. Therefore, the time to print one layer is 17×10 /7.41 sec = 22.92 sec. Multiplying this with 27 gives us the total print time of 10.31 minutes. This gives us the effective mass flow rate that is responsible for fabricating the component and it comes out to be 7400/(10.31×60) mg/s ≈11.96 mg/s. Since the spatter rate as estimated from the video is 1.58 mg/s, the total mass of powder that enters the melt pool per second is equal to the sum of material that is utilized for printing the part and the amount of material lost as spatters. This turns out to be 13.54 mg/s. We call this the effective flow rate. We now have the proportion of the effective flow rate that is ejected out as spatter and is equal to 1.58/13.54=11.67%. Comparing this effective flow rate with the nominal flow rate of 124.08 mg/sec, we note that the amount of powder that is wasted (i.e., without entering the melt pool) is (1-13.54/124.08) × 100 % = 89.09% of the total powder exiting the nozzle.

Based on the above numerical calculations, the powder capture efficiency of the L-DED process is less than 10%. This is not surprising as the reported literature on L-DED suggests that the powder capture efficiency is generally low, with values ranging between 7.5% to 15% [32-34]. For instance, with a laser power of 350W, a scan speed of 14.82 mm/sec, and a powder feed rate of 142 mg/sec, authors in [32] found the powder capture efficiency to be 7.5%. Since the laser power and powder feed rates are comparable to our experiments, the difference in the capture efficiency may be attributed to the difference in the scan speed (14.82 mm/sec in [32] vs. 7.41 mm/sec in this work). Since increasing scan speed reduces the powder capture [43], we note a lower powder capture efficiency in [32]. In another study a laser power of 325W and powder feed rate of 66 mg/sec, the capture efficiency was reported to be 10% [34]. No information on the scan speed was provided in this work.

While some recent studies have investigated the powder capture efficiency, spatter quantification is still an open area of research with only a handful of works outside of L-DED. For instance, Raza et al. analyzed the spatter rate in laser powder bed fusion to be below 3.5% [44]. However, it is not appropriate to compare the spatter rates for different systems, and more work is necessary to characterize the spatter formation in the L-DED process. Subsequent studies are also necessary to establish the effect of the process parameters on the spatter rate and, eventually the build quality

6. Conclusions

Towards monitoring the deposition of material in the L-DED process, we developed a high-speed imaging system capable of recording the IR signatures of the melt pool dynamics and spatter particles. In this work, we particularly focused on the spatter particles—the molten material that is ejected out of the deposition zone, including the melt pool. We first develop a Kalman filter to track, in real-time, the spatter particles and then record their trajectories. Using this information, we estimate the spatter count and spatter rate. We note that a significant portion (89%) of the powder material is wasted even before entering the melt pool. Out of the remaining 11% of the powder particles that enter the deposition zone, approximately 12% of the material is ejected out via spattering.

From the calculation presented in the foregoing, we also note that several processing parameters, including the powder flow rate, scan speed, etc., influences the spatter rate and, therefore, the build quality. We are currently investigating the effect of various process parameters such as the laser power on the spatter rate and consequently on the build quality. Future works will also investigate the ability to control the process parameters in real-time that would minimize the spatter formation. We also note some limitations of the present study. First, the limitations associated with the Kalman filter that assumes that the system is evolving linearly may be accurate, especially in the case of spatter, whose makeup may change from liquid to solid as it entrains away from the melt-pool. This limitation may be addressed by using non-linear versions of the Kalman filter. Another limitation of the current work is that the process is only monitored using a single camera which only provides a projection of the three-dimensional spattering process on a two-dimensional plane. This may also lead to an underestimation of the spatter. Finally, we also note that with the current imaging setup, we are unable to distinguish between spatter and plumes. Future studies will also focus on characterizing the differences between spatter and plumes to estimate the spatter rate accurately.

Acknowledgements

The authors acknowledge the kind support from the Texas A&M President's X-grant and NSF S&AS 1849085.

Appendix A. Ring method and velocity vector method

Ring method: In the "ring" method, a ring centered at the melt pool is used to count the particles by checking if the particles cross it in the successive frames, as shown in Fig. 6.

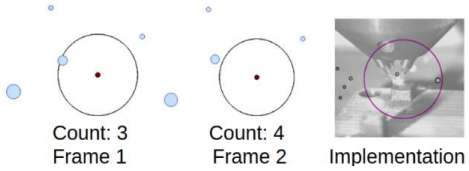

Fig. 6. schematic for spatter count using ring method

Relative position method: In the tracking method, we track the complete particle trajectory from start to end in order to get the spatter count. The tracking process is visually shown in Fig. 7 where, 'O' is the position of the particle in 1st frame; 'P' is the position of the particle in 2nd frame; 'Q' is the linearly predicted position in 3rd frame; 'R' shows the actual position of the predicted particle in 3rd frame. The algorithm is initialized by assigning the position of the spatter in the successive frame by finding the closest spatter in the radial direction from the melt pool. In Fig. 6, 'P' shows the position of the initialized spatter, using coordinates of 'O' and 'P', straight-line parameters r and θ can be calculated. Using r and θ we can predict the spatter position in the next frame, i.e., position 'Q'. The actual position is known by finding the closest position to the spatter in that frame. Once the actual position 'R' is known, the parameters r and θ are updated, and prediction for the next frame continues.

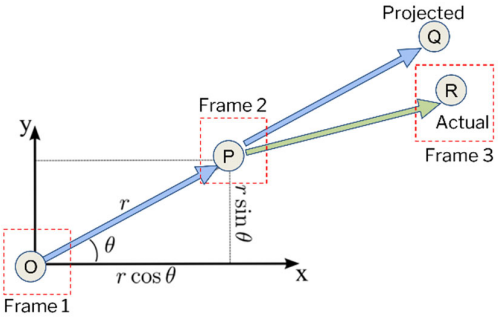

Fig. 7. schematic for spatter tracking algorithm

References

[1]. Botcha, B., et al. Implementing the Transformation of Discrete Part Manufacturing Systems Into Smart Manufacturing Platforms. in ASME 2018 13th International Manufacturing Science and Engineering Conference. 2018. American Society of Mechanical Engineers Digital Collection.

[2]. Gibson, I., D.W. Rosen, and B. Stucker, Additive manufacturing technologies. Vol. 17. 2014, New York: Springer.

[3]. Wolff, S.J., et al. In-situ high-speed X-ray imaging of piezo-driven directed energy deposition additive manufacturing. Scientific reports 2019; 9(1): p. 962.

[4]. Thompson, S.M., et al. An overview of Direct Laser Deposition for additive manufacturing; Part I: Transport phenomena, modeling and diagnostics. Additive Manufacturing 2015; 8: p. 36-62.

[5]. Peyre, P., et al. Analytical and numerical modelling of the direct metal deposition laser process. Journal of Physics D: Applied Physics 2008; 41(2): p. 025403.

[6]. Ly, S., et al. Metal vapor micro-jet controls material redistribution in laser powder bed fusion additive manufacturing. Scientific reports 2017; 7(1): p. 4085.

[7]. Mumtaz, K. and N. Hopkinson. Selective laser melting of thin wall parts using pulse shaping. Journal of Materials Processing Technology 2010; 210(2): p. 279-287.

[8]. Naesstroem, H., F. Brueckner, and A.F. Kaplan. Blown powder directed energy deposition on various substrate conditions. Journal of Manufacturing Processes 2022; 73: p. 660-667.

[9]. Prasad, H.S., F. Brueckner, and A.F. Kaplan. Powder incorporation and spatter formation in high deposition rate blown powder directed energy deposition. Additive Manufacturing 2020; 35: p. 101413.

[10]. Matthews, M.J., et al. Denudation of metal powder layers in laser powder bed fusion processes. Acta Materialia 2016; 114: p. 33-42.

[11]. Melvin III, L.S., S. Das, and J. Beaman Jr Jr. Video Microscopy of Selective Laser Sintering. in 1994 International Solid Freeform Fabrication Symposium. 1994.

[12]. Kruth, J.-P., et al. On-line monitoring and process control in selective laser melting and laser cutting. in Proceedings of the 5th Lane Conference, Laser Assisted Net Shape Engineering. 2007.

[13]. Schwerdtfeger, J., R.F. Singer, and C. Körner. In situ flaw detection by IR-imaging during electron beam melting. Rapid Prototyping Journal 2012; 18(4): p. 259-263.

[14]. Berumen, S., et al. Quality control of laser-and powder bed-based Additive Manufacturing (AM) technologies. Physics procedia 2010; 5: p. 617-622.

[15]. Craeghs, T., et al. Determination of geometrical factors in Layerwise Laser Melting using optical process monitoring. Optics and Lasers in Engineering 2011; 49(12): p. 1440-1446.

[16]. Lott, P., et al. Design of an optical system for the in situ process monitoring of selective laser melting (SLM). Physics Procedia 2011; 12: p. 683-690.

[17]. Chivel, Y. and I. Smurov. On-line temperature monitoring in selective laser sintering/melting. Physics Procedia 2010; 5: p. 515-521.

[18]. Clijsters, S., et al. In situ quality control of the selective laser melting process using a high-speed, real-time melt pool monitoring system. The International Journal of Advanced Manufacturing Technology 2014; 75(5-8): p. 1089-1101.

[19]. Hua, T., et al. Research on molten pool temperature in the process of laser rapid forming. Journal of Materials Processing Technology 2008; 198(1-3): p. 454-462.

[20]. Montazeri, M., et al. In-process monitoring of porosity in additive manufacturing using optical emission spectroscopy. IISE Transactions 2019: p. 1-16.

[21]. Bi, G., C. Sun, and A. Gasser. Study on influential factors for process monitoring and control in laser aided additive manufacturing. Journal of Materials Processing Technology 2013; 213(3): p. 463-468.

[22]. Tang, L., et al. Variable powder flow rate control in laser metal deposition processes. Journal of Manufacturing Science and Engineering 2008; 130(4): p. 041016.

[23]. Hofmeister, W., G.A. knorovsky, and D.O. maccallum, Video monitoring and control of the LENS process. 1999, Sandia National Labs., Albuquerque, NM (US).

[24]. Chen, Y., et al. Melt pool morphology in directed energy deposition additive manufacturing process. in IOP Conference Series: Materials Science and Engineering. 2020. IOP Publishing.

[25]. Nassar, A., B. Starr, and E. Reutzel. Process monitoring of directed-energy deposition of Inconel-718 via plume imaging. in 2014 International Solid Freeform Fabrication Symposium. 2015. University of Texas at Austin.

[26]. Ermurat, M., et al. Process parameters investigation of a laser-generated single clad for minimum size using design of experiments. Rapid Prototyping Journal 2013; 19(6): p. 452-462.

[27]. Balu, P., P. Leggett, and R. Kovacevic. Parametric study on a coaxial multi-material powder flow in laser-based powder deposition process. Journal of Materials Processing Technology 2012; 212(7): p. 1598-1610.

[28]. Haley, J.C., J.M. Schoenung, and E.J. Lavernia. Observations of particle-melt pool impact events in directed energy deposition. Additive Manufacturing 2018; 22: p. 368-374.

[29]. Jeon, I., et al. Online melt pool depth estimation during directed energy deposition using coaxial infrared camera, laser line scanner, and artificial neural network. Additive Manufacturing 2021; 47: p. 102295.

[30]. Botcha, B., A.S. Iquebal, and S.T. Bukkapatnam. Smart manufacturing multiplex. Manufacturing Letters 2020; 25: p. 102-106.

[31]. Zekovic, S., R. Dwivedi, and R. Kovacevic. Numerical simulation and experimental investigation of gas–powder flow from radially symmetrical nozzles in laser-based direct metal deposition. International Journal of Machine Tools and Manufacture 2007; 47(1): p. 112-123.

[32]. Katinas, C., et al. Modeling particle spray and capture efficiency for direct laser deposition using a four nozzle powder injection system. Journal of Manufacturing Science and Engineering 2018; 140(4).

[33]. Katinas, C., S. Liu, and Y.C. Shin. Self-sufficient modeling of single track deposition of Ti–6Al–4V with the prediction of capture efficiency. Journal of Manufacturing Science and Engineering 2019; 141(1).

[34]. Liu, Z., et al. Analytical modeling and experimental validation of powder stream distribution during direct energy deposition. Additive Manufacturing 2019; 30: p. 100848.

[35]. Tapia, G. and A. Elwany. A review on process monitoring and control in metal-based additive manufacturing. Journal of Manufacturing Science and Engineering 2014; 136(6): p. 060801.

[36]. Iquebal, A.S., B. Botcha, and S. Bukkapatnam. Towards rapid, in situ characterization for materials-on-demand manufacturing. Manufacturing letters (In Press) 2019.

[37]. Botcha, B., A. Iquebal, and S. Bukkapatnam. Smart manufacturing multiplex. Manufacturing Letters (Under review) 2019.

[38]. Soille, P., Morphological image analysis: principles and applications. 2013: Springer Science & Business Media.

[39]. Kalman, R.E. A new approach to linear filtering and prediction problems. Journal of basic Engineering 1960; 82(1): p. 35-45.

[40]. Yagoh, K., K. Ogawara, and S.-i. Iida, The particle tracking method using the kalman filter, in Flow Visualization VI. 1992, Springer. p. 838-842.

[41]. Heeling, T., M. Gerstgrasser, and K. Wegener. Investigation of selective laser melting spatter characteristics for single-and multi-beam strategies using high speed imaging. in Lasers in Manufacturing Conference (LiM 2017). 2017. Wissenschaftliche Gesellschaft Lasertechnik eV (WLT).

[42]. Liu, Y., et al. Investigation into spatter behavior during selective laser melting of AISI 316L stainless steel powder. Materials & Design 2015; 87: p. 797-806.

[43]. Akinlabi, E.T., et al. Effect of scanning speed on material efficiency of laser metal deposited Ti6Al4V. World Academy of Science and Technology, Paris 2012; 6: p. 58-62.

[44]. Raza, A., et al. Degradation of AlSi10Mg powder during laser based powder bed fusion processing. Materials & Design 2021; 198: p. 109358.